



Article

Experimental Analysis and Spatial Component Impact of the Inert Cross Flow in Open-Architecture Laser Powder Bed Fusion

Magnus Bolt Kjer * , Zhihao Pan, Venkata Karthik Nadimpalli * and David Bue Pedersen

Department of Civil and Mechanical Engineering, Technical University of Denmark, 2800 Kgs. Lyngby, Denmark; zhipa@dtu.dk (Z.P.); dbpe@dtu.dk (D.B.P.)

* Corresponding author: mbokj@dtu.dk (M.B.K.); vkna@dtu.dk (V.K.N.)

Abstract: Laser-based powder bed fusion is an additive manufacturing process in which a high-power laser melts a thin layer of metal powder layer by layer to yield a three-dimensional object. An inert gas must remove process byproducts formed during laser processing to ensure a stable and consistent process. The process byproducts include a plasma plume and spatter particles. An NC sensor gantry is installed inside a bespoke open-architecture laser-based powder bed fusion system to experimentally characterize the gas velocity throughout the processing area. The flow maps are compared to manufactured samples, where the relative density and melt pools are analyzed, seeking a potential correlation between local gas flow conditions and the components. The results show a correlation between low gas flow velocities and increased porosity, leading to lower part quality. Local flow conditions across the build plate also directly impact components, highlighting the importance of optimizing the gas flow subsystem. The experimental flow analysis method enables optimization of the gas flow inlet geometry, and the data may be used to calibrate the computational modeling of the process.

Keywords: L-PBF; metal laser powder bed fusion; cross flow; shielding gas; experimental anemometry



Citation: Kjer, M.B.; Pan, Z.; Nadimpalli, V.K.; Pedersen, D.B. Experimental Analysis and Spatial Component Impact of the Inert Cross Flow in Open-Architecture Laser Powder Bed Fusion. *J. Manuf. Mater. Process.* **2023**, *7*, 143. <https://doi.org/10.3390/jmmp7040143>

Academic Editors: Hamed Asgari and Elham Mirkoohi

Received: 6 July 2023

Revised: 28 July 2023

Accepted: 2 August 2023

Published: 7 August 2023



Copyright: © 2023 by the authors. Licensee MDPI, Basel, Switzerland. This article is an open access article distributed under the terms and conditions of the Creative Commons Attribution (CC BY) license (<https://creativecommons.org/licenses/by/4.0/>).

1. Introduction

Laser powder bed fusion (L-PBF) is an additive manufacturing (AM) process that employs a laser to selectively consolidate layers of sub-millimeter powder. The laser systematically melts the powder layer by layer, stacking two-dimensional patterns to fabricate three-dimensional objects. Known for their geometric freedom and ability to process traditionally challenging alloys, powder-bed-based AM processes tend to cause a relatively high cost per manufactured component [1,2]. L-PBF is a well-established process with a broad range of applications within diverse industries, including but not limited to the medical [3] and aerospace sectors [4]. L-PBF started in niche and high-cost, high-performance sectors. Nevertheless, the AM industry (products and services) had an estimated revenue of USD 15.2 billion in 2021 and has experienced yearly growth of almost 20% per year for several years, partly due to the increasing number of applications [5].

1.1. L-PBF Process Parameters

Achieving a satisfactory component using any metal L-PBF system demands precise control over several process variables and subsystems. The current work primarily focuses on the inert shielding gas's cross flow across the processing area. Besides the gas flow, the volumetric energy density (VED) is a frequently used measure that encapsulates most of the critical parameters that operators can control in commercial systems[6].

$$VED = \frac{P}{hvt} \quad (1)$$

The *VED* is defined by Equation (1), where P represents the laser power in watts, h is the hatch spacing in millimeters, v signifies the scan speed in mm/s, and t denotes the layer thickness in millimeters. It is important to note that *VED* is not easily transferable across systems and tends to vary among alloys [7], and while the *VED* can be a helpful heuristic, it is the subject of valid criticism [6]. Variables such as beam spot diameter, shielding gas type, and build plate temperature impact the required process parameters and the resulting component. The gas flow profile and velocity are critical process variables that require optimization and analysis to ensure consistent samples and a stable system.

When the intense heat of the laser spot impinges on the powder, regions of the melt pool may reach temperatures above the boiling point of the metal, causing the rapidly expanding metal vapor to form a plume. This causes partially melted particles and fully melted droplets to shoot outwards. Unmelted powder particles can also be entrained in the flow [8,9]. The process byproducts relevant to the gas flow can be coarsely divided into spatter and plume formations. Both are affected by the shielding gas flow.

It has been shown that the shielding gas flow velocity can affect the porosity of the components [10–12] and the process parameters necessary to successfully achieve fully dense components. When using and designing a metal L-PBF system, it is vital to holistically and individually understand and investigate the effect of each subsystem that constitutes part of the entire system.

1.2. Spatter

The powder laser welding process gives rise to a plume and ejected particles. These spatter particles, typically larger in diameter than the powder feedstock, assume a spherical shape. Spatter, a common occurrence in welding processes, is characterized as a substance transitioning from a liquid to a solid state that adheres to the substrate. It usually shares similar composition with the original feedstock [13]. The spatter formation is believed to be a result of melt pool instabilities. The recoil pressure, Marangoni effect, and the heat effect in the molten each result in three different spatter types and spatter morphologies [14]. The sizes of the spatter particles also impact the degree to which the gas flow is able to entrain the particles. Ejected powder particles represent a feature somewhat unique to L-PBF, wherein the powder feedstock experiences local drag forces due to the flow conditions present in the heated melt pool [8,9].

The ejected particle types can form detrimental buildups if remelted by the laser, ultimately leading to, e.g., recoater collisions and insufficient powder layers due to an increased top-surface roughness. It can also result in trapped impurities and porosities. The scattering of the impinging laser beam may even cause balling, starting a process whereby the redeposits grow with each subsequent layer [15]. Recent work indicates that the spatter can be largely eliminated by adopting finer process control. Controlling the laser power using a linear ramping of the laser power during the first 300 μs had a significant impact [16].

1.3. The Plume

The plasma plume forms in the laser–powder interaction zone, where the laser ionizes the atmosphere. In addition, it contains vaporized metal, which rapidly cools and condenses into nanometer-sized particles (10–150 nm). The vapor plume is ejected at remarkably high speeds proportionate to the laser power, reaching several hundreds of meters per second. The velocity decreases exponentially and, after rising 0.5–2 mm in height, approaches a velocity of 100 m/s [8]. The atomic weight of the shielding gas and the pressure are believed to affect the spatter quantity, along with the plume velocity and size; elevated pressures and lighter gasses can decrease the amount of spatter. The higher pressure helps form slower subsonic plumes by reducing evaporation. The lighter gasses increase the gas-entrainment velocity and decrease the jet radius. This is hypothesized to force the entrained particles to be absorbed by the melt pool [17]. The gaseous environment could be considered on par with the conventional process parameters used in the volumetric energy density.

If the plume is not adequately removed from the processing zone, it will reduce the incident laser power, decreasing the actual process parameters and causing defects. The scan direction relative to the flow direction and, therefore, the direction of the plume also influence the laser input. A perpendicular scanning direction relative to the cross-flow direction is preferred [9].

A proposed better description of the laser and powder interaction is the normalized enthalpy. It is used to consider the differences in thermal and optical properties among different materials and directly encompasses aspects such as the beam diameter, as opposed to the volumetric energy density (Equation (1)). The normalized enthalpy more directly considers the complex interface between the laser radiation, the substrate (powder feedstock), and, in a sense, the environment. The normalized enthalpy is expressed by Equation (2) [18],

$$\overline{\Delta H} = \frac{\Delta H}{\Delta h} = \frac{\alpha P}{\rho(C\Delta T + L_m)\sqrt{\pi\omega^3 VD}} \quad (2)$$

where α is the absorptivity of the bulk material, P is the laser power (W), ρ is the density (kg/m^3), C is the specific heat (J/kgK), ΔT is the difference between the melting and initial temperatures (K), L_m is the latent heat of melting (kJ/kg), ω is the laser spot radius (m), V is the laser speed (m/s), D is the thermal diffusivity (m^2/s), and d is the melt pool depth (m). Not only is the effective power (P) reduced by the particles blocking the incident radiation [15], but the effective spot size (ω) is altered due to the scattering caused by the plume. A larger or irregularly shaped spot decreases the energy density and may lead to defects [15]. Besides the large-scale properties of the flow, local flow circumstances may create regions with suboptimal results, thus highlighting the immediate need to address the cross flow of the inert gas.

1.4. Cross-Flow Requirements and Flow Conditioners

Uniformity is key in L-PBF when designing the gas flow. The gas flow should be homogeneous over the entire building surface. This includes a defined orientation of the gas flow and a constant gas flow velocity in all areas [19] where a sufficient gas velocity covers every region. Critically, the velocity in the z direction should be minimized and, ideally, approach zero [20].

The optimal specific velocities and the height of a given velocity vector above the powder bed are, at the moment, undefined. However, the gas flow should have a high velocity while staying in the laminar flow regime; however, higher velocity leads to instability and results in turbulence. Flow conditioners are employed in wind tunnels to battle turbulence, where similar requirements apply. A settling duct or chamber with flow conditioners like honeycomb and screens improves the flow. The honeycomb improves flow uniformity by aligning the flow with the axis of the pipe and decreasing larger-scale flow unsteadiness. The incoming flow should enter the honeycomb at a yaw angle of $<10^\circ$ to avoid stalling across the honeycomb surfaces. The cells can be circular (typically seen in commercial L-PBF systems); however, in wind tunnels, they are often hexagonal, as they have been found to decrease the pressure drop. The best-performing cells have length-to-width ratios of 7–10. Screens can break larger-scale turbulence into smaller sizes so that the larger turbulent eddies are reduced to smaller eddies, which then decay [21]. The inlet geometry prototype used in this work was manufactured using polymer material extrusion AM with a honeycomb structure.

Reijonen et al. [11] found that the velocity on the build plate was ≈ 0.5 m/s (using a hot wire probe) or higher before a decrease in porosity was observed. In contrast, Shen et al. [12] found velocities of 4 m/s and more at the build plate (measured using a vane flow meter) caused powder denudation and volume loss in the powder bed.

Besides flow conditioners, the placement and dimensions of the inlet geometry are vital. Elkins et al. [22] found that the height of the inlet may cause a low-pressure zone between the incoming flow and the bottom surface, where vortices are formed due to

the backward-facing flow step effect. Adding a secondary lower flow resolved the issue. Similarly, Zhang et al. [20] found that placing the inlet above the build plate may cause a downward velocity due to the Coandă effect. The vertical movement of the gas may deposit the spatter closer to the processing area rather than carrying the byproducts away. Besides the height relative to the build plate, flow conditioners may reduce these detrimental flow behaviors. Yang et al. [23] demonstrated the effect of using flow conditioners on the cross flow's ability to pick up the byproducts.

- The gas flow velocity should be as high as possible to optimize the removal of the process byproducts and to avoid redeposits;
- The flow should be as close to the powder bed as possible to minimize the interaction between the laser and the byproducts;
- Flow separations and turbulence resulting in velocity in the z direction should be reduced to a minimum to decrease the probability of disturbances of the laser beam path by process byproducts;
- The flow velocity profile should not disturb or otherwise entrain the powder bed;
- The height of the flow profile should be sufficient to avoid ejecta escaping the cross flow.

1.5. Gas Flow Analysis

Metal L-PBF is fundamentally a welding process, embodying the standard challenges of laser welding and certain unique obstacles. When the incident laser beam encounters the powder, it induces a melt pool that traces the laser's trajectory. Throughout this process, a condensate plume and weld spatter are generated, which are swept away by the gas flow, simultaneously shielding the weld pool from oxygen exposure [9].

Analysis of the gas flow is conducted by spatially mapping the cross flow using an integrated, custom NC sensor platform. The method of using a flow probe (anemometer) to establish the velocity field for cross-flow analysis in L-PBF was developed by Schniederharn et al. [24]. Several seconds of data are averaged, and the resulting flow map is then an interpolation of each measurement in 3D space. The method facilitates flow analysis under conditions identical to those of manufacturing [10,25] and is found to be repeatable. In an alternative strategy, a volumetric methodology has been developed using magnetic resonance velocimetry, allowing for non-intrusive analysis of the fluid system [22]. This method allows for analysis of turbulence and velocities. However, careful compensation must be performed when using a different fluid. Additionally, qualitative flow analysis is possible using Schlieren imagery, which makes complex turbulent behavior, vortices, and melt pool ejecta visible. Schlieren also works with high-speed imagery, which provides a different perspective of the chaotic process [9].

While computational fluid dynamics are not utilized in the current work, the experimental method shall be considered a supplement. Computational methods facilitate rapid iteration of the design aspects of the flow geometry. Experimental models are nevertheless valuable for holistically characterizing the flow system. Moreover, the flow maps can serve as calibration data for computational models, enhancing the model's validity.

2. Materials and Methods

The work is carried out on a bespoke open-architecture, open-source L-PBF system (full source to be found at <https://github.com/DTU-OpenAM/OpenAM-PBF>, fully published January 2024) that functions as a production machine with complete experimental freedom. The subsystems are designed or purchased for process control using standard interfaces and modular designs.

Three datasets were collected and analyzed individually and comparatively: (1) the spatially resolved gas velocity, (2) the manufactured component density, and (3) the melt pool. The flow measurement maps were made to characterize the flow experimentally, while the manufactured components were used to gauge the effectiveness of the cross-flow process parameter.

2.1. Flow Measurements

Figure 1 shows the L-PBF system processing chamber with the automated flow probe platform. The location of each flow measurement and component position relative to the 250 mm diameter build plate can be seen in Figure 2, with a total of 65 flow positions per measured plane and 13 planes spaced 5 mm to 60 mm above the build plate.

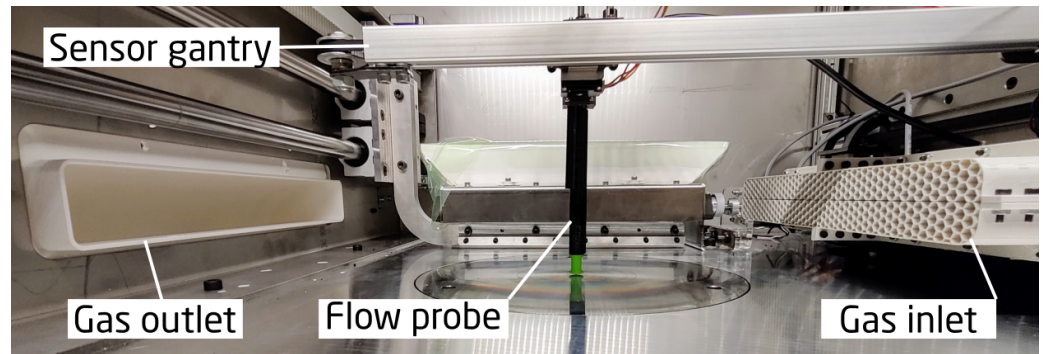


Figure 1. Photo of inside the L-PBF machine with the honeycomb prototype, gas outlet, and flow probe attached to the sensor gantry.

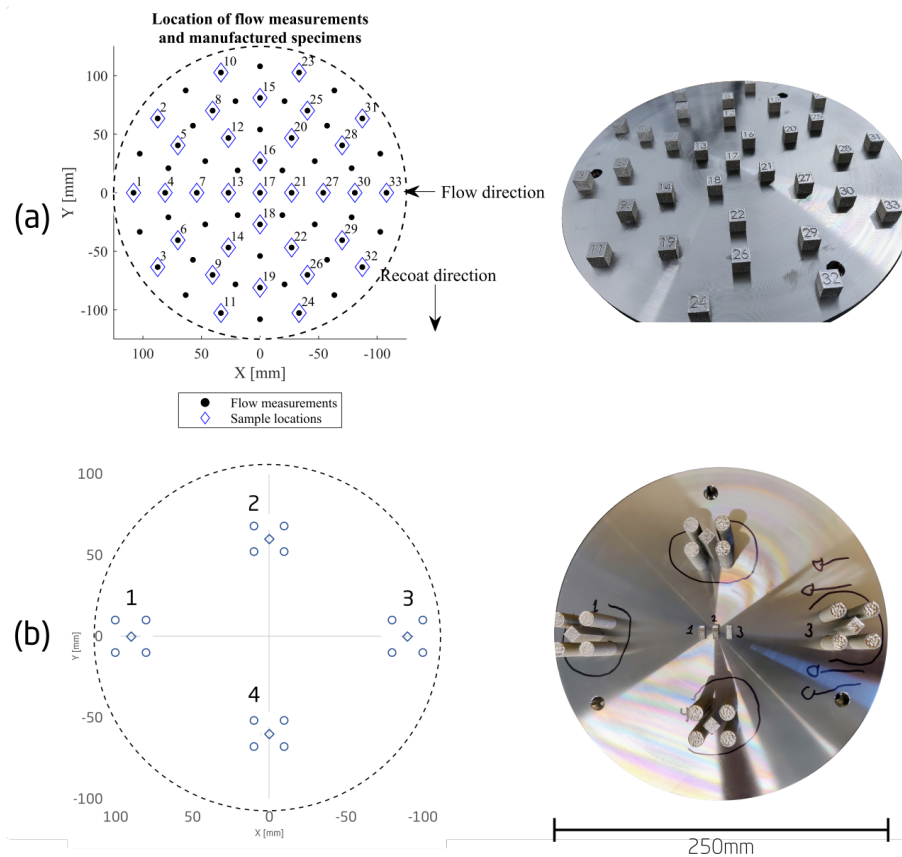


Figure 2. Location of each flow measurement and sample placements. (a) Numbering indicates the scan ordering within each layer. (b) Numbering indicates sample clusters.

The system used to measure the flow was described in [26], consisting of a 3-axis NC sensor platform controlled using an ATmega 8-bit 16 MHz microcontroller. An EE671 (Epluse, Engerwitzdorf, Austria) miniature air flow probe was used to measure the flow velocity within a range of 0–15 $\frac{m}{s}$, with a stated accuracy of ± 0.2 m/s and an analog output

of 0–10 V. The cross-sectional area in which the sensor measures is 10 mm × 10 mm. It was calibrated using the differential pressure measured using a micromanometer [24].

$$v = \sqrt{\frac{2 \cdot \Delta p}{\rho}} \quad (3)$$

where v is the velocity at the placement of the probe in m/s, Δp is the differential pressure in Pa, and ρ is the density of the gas in $\frac{\text{kg}}{\text{m}^3}$.

A National Instruments NI 9215 data acquisition module was used to collect the 0–10 V analog signal, along with the trigger signal from the ATmega controller.

It was decided to use a set of concentric circles to fill the plate due to the round build plate. A collection time of 5 s per location was used at a collection frequency of 100 Hz. The measured values were extracted using Python, and the plotting was carried out in Matlab, where a 2D interpolation of the data with a grid size of 0.5 mm × 0.5 mm approximated the data as a 2D flow plane.

2.2. Manufacturing

A perfect gas flow is unquantifiable, as it depends on many factors, including the flow-shaping geometry, process parameters, the inert gas, chamber pressure, direction relative to the scan direction, etc. Rather than a global optimum, a plethora of local maxima is assumed to be possible, each producing excellent components. However, the global minimum must be no gas flow.

Therefore, half of the gas inlet was covered, and the flow system was set to the lowest setting possible, referred to as “slow.” This was done to benchmark the performance and its impact. A section of the flow was uncovered to avoid system damage and ensure a proper overall oxygen level during manufacturing.

Next, two print designs were made to analyze the gas flow’s impact on the components. First, 33 cubes filled the build plate. The cubes were rotated 45° relative to the recoater direction, as a square edge can be detrimental to forming a proper powder layer. Their placements are shown relative to the system controller’s coordinate system in Figure 2. This was done to test for a correlation between the gas flow velocity and specimen placement on the build plate with a relatively high spatial resolution. The manufactured samples are seen in Figure 2.

Then, 4 clusters of cylinders were manufactured to highlight the macro effect of the gas flow. The same design was used for the job without gas flow.

The processing parameters were found to produce dense cuboids under acceptable flow conditions. The parameters are shown below in Table 1, equating to $VED_{cubes} = 92.6 \frac{\text{J}}{\text{mm}^3}$ and $VED_{cylinders} = 76.9 \frac{\text{J}}{\text{mm}^3}$, which are comparable to previously reported values [7]. The system has a laser spot size of 90 μm and was printed without build-plate preheating, using nitrogen as the inert atmosphere with an oxygen level below 0.1%. The powder used in all the experiments was gas-atomized 316 L stainless steel (Höganäs, Höganäs, Sweden), with a nominal particle range of 20–53 μm.

Table 1. Processing parameters used for the two sets of experimental designs.

Job	Scan Velocity	Laser Power	Hatch Spacing	Layer Thickness	VED
Cubes	600 mm/s	250 W	90 μm	50 μm	92.6 Jmm ³
Cylinders	650 mm/s	250 W	100 μm	50 μm	76.9 Jmm ³

2.3. Density Measurements

All the samples’ relative densities were measured using the Archimedes method. A Sartorius BP210S (Struers, Ballerup, Denmark) 1 mg balance was employed, using

a Sartorius YDK density kit with ethanol as the medium. By comparing the buoyancy in air and ethanol, the overall density can be found using the following equation:

$$\rho = \frac{W_a(\rho_{fl} - \rho_a)}{C(W_a - W_{fl})} + \rho_a \tag{4}$$

where W_a and W_{fl} are the weight in air and the fluid medium, respectively; ρ_a is the density of air; ρ_{fl} is the density of the fluid medium; and $C = 0.99983$ is a correction factor specific to the density kit.

2.4. Melt-Pool Dimensions

All cubes were cut perpendicularly to the laser direction of the topmost layer. The samples were prepared by grinding using 500, 1000, and 4000 grit SiC papers, followed by chemical polishing using Struers DiaPro Mol B 3µm, DiaPro Nap B 1 µm, and oxide polishing suspensions. The prepared samples were etched using Krolls reagent for 30 min and investigated using a Zeiss Axio light optical microscope. The melt pools were measured based on multitrack morphology in the topmost layer using ImageJ software.

3. Results

First, the flow maps are presented and, thereafter, compared to the manufactured components.

3.1. Flow Maps

The velocities are controlled by a closed-loop control, wherein a flow meter measures the gas flow before entering the enclosure. Three settings are used in this study, and as this value is dissimilar to the actual velocities across the processing area, these will henceforth be referred to as fast, medium, and slow. The maximum speed in the middle of the flow near the inlet was 5.1 m/s using the fast setting, 2.5 m/s using the medium setting, and 1.2 m/s with the slow setting. The interpolated velocity maps in Figure 3 show a distinct dissimilarity between the chosen settings.

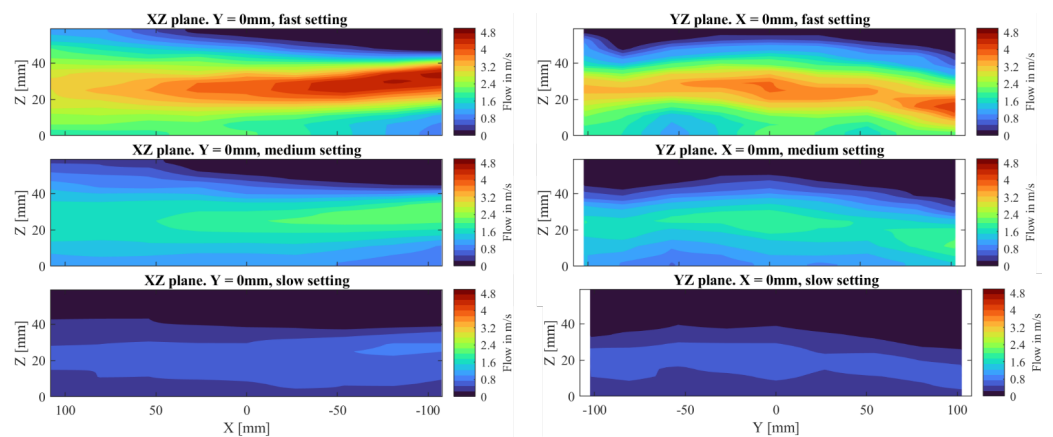


Figure 3. X–Z and Y–Z flow maps.

Comparing the settings in Figure 3, the gradient is steeper in the fast flow, with the highest velocities in the middle. The overall shape of the flow is also largely unchanged with increasing speed, which is particularly clear when cutting the data along the YZ plane in the right of Figure 3. Attaining a spatially consistent flow through time and speed settings is beneficial, as it reduces process variation. The uniform flow along the X and Y directions must be ideal for the process parameters to behave consistently throughout the processing area. The velocities can be seen to be uniform in the y direction, i.e., along the flow inlet. A gradient in the x direction as the flow expands, i.e., in the direction of flow, is clear and expected. Extending the shielding gas outlet (to the left on the XZ plane) to

be closer to the processing area could minimize this effect, which would reduce the flow distance. The XZ planes clearly show an unwanted downward movement of the cross flow and a low-velocity zone in the bottom-right corner of the plots. This is caused by the inlet being above the build plate.

The XY flow maps (Figure 4) similarly reveal a low-velocity region at $z = 0$ near $x = -100$ mm, especially in the medium and fast settings. The slow setting is more uniformly near zero throughout $z = 0$.

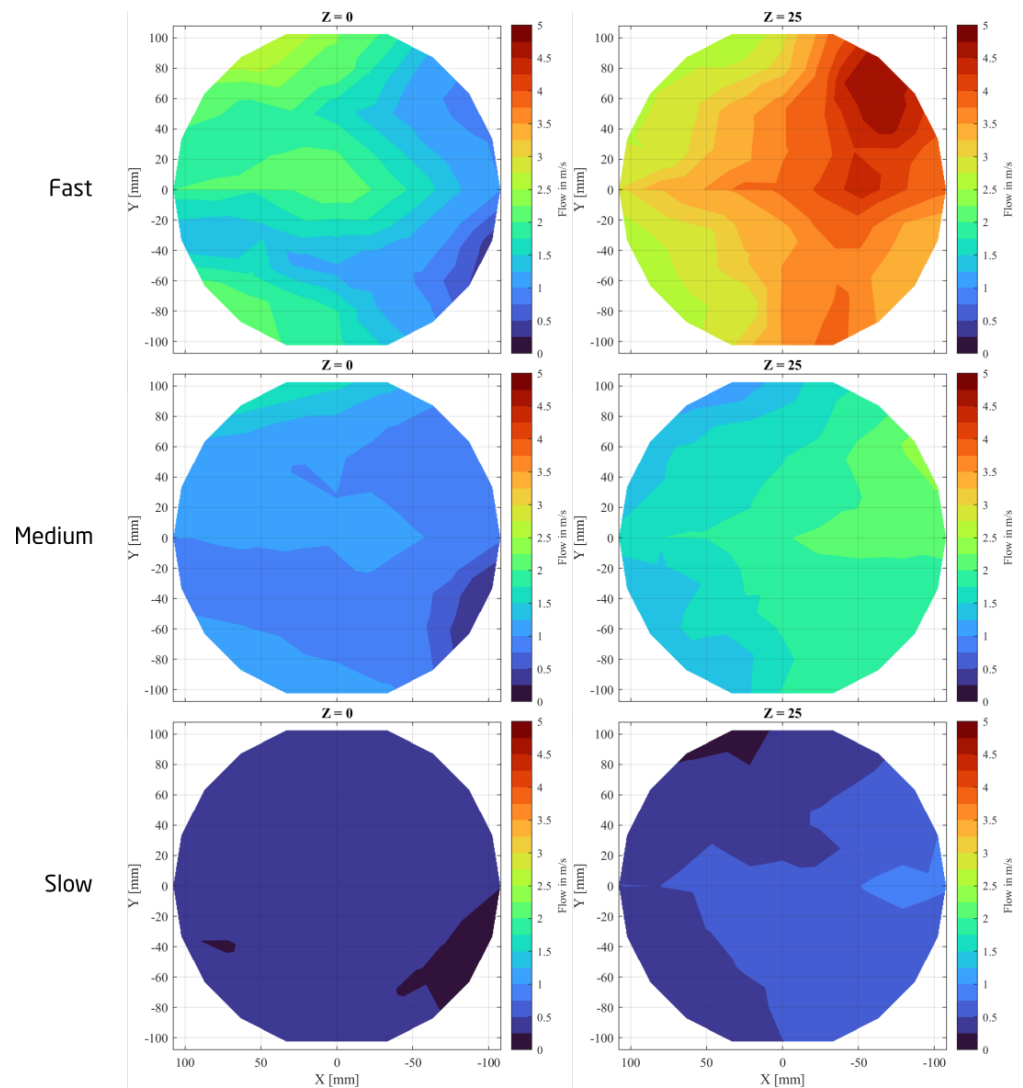


Figure 4. X–Y flow maps.

Whereas the flow maps above are qualitative, the interplane comparison using the mean velocities is more explicit (Figure 5a). The velocity at $z = 0$ is possibly an important parameter, as the byproducts should be (re)moved as soon as possible to avoid disrupting the process. The intraplanar variation in flow speed also follows a predictable pattern, with more variation as the gas flow increases, as shown in Figure 5b. A higher degree of irregularity may indicate a more chaotic and unstable flow condition, where turbulence may entrap the plume.

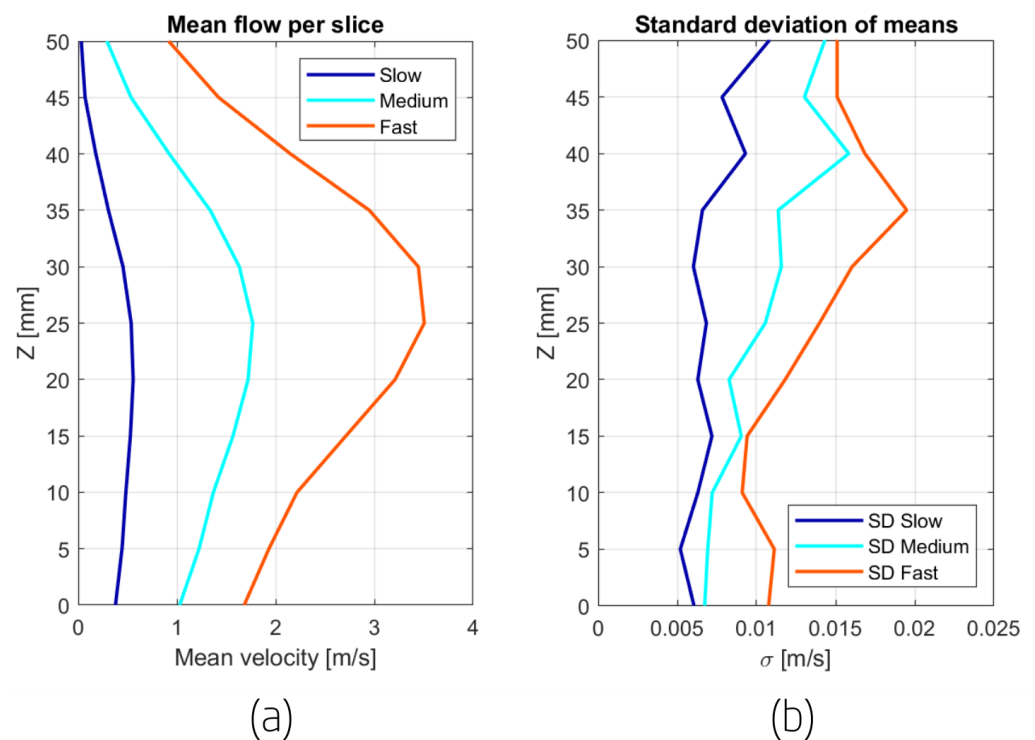


Figure 5. (a) The mean flow velocities of each measured plane and (b) each plane's standard deviation.

3.2. Bulk Density

The bulk density provides an unspecific macro-level metric for each component.

3.2.1. Cubes

The bulk densities attained using the Archimedes principle described above can be seen in Figure 6. The sample density and location in the y direction exhibit no strong correlation, consistent with the uniform flow in the YZ plane as depicted in Figure 3. Despite the slightly lower density along the negative y direction, the marginal variation in the flow does not impact energy input significantly. However, a trend along the x direction is discernible, primarily in the fast setting and, to a lesser extent, in the lower setting. Higher densities tend to be found further away from the inlet. The velocity is expected to correlate with dense components—up to a point. Possible detrimental effects from a fast flow, as introduced above, may include turbulence and powder denudation. The data indicate that the gas flow needs a velocity of 0.5–1 m/s or more to meaningfully impact the byproducts near the powder bed, which is consistent with the findings reported in the literature.

3.2.2. Cylinders

Each cluster is presented by its average densities and corresponding standard deviation error bars for the second experimental design. Figure 7 reveals a similar trend, as above, when the densities are plotted with respect to the location in the x direction. While the clusters near the outlet ($x \approx 100$) are not significantly different using the fast and medium settings, they show some of the largest variations. The clusters near the inlet ($x \approx -100$) are denser with a faster flow setting. Neither of the settings reveals a robust linear fit, as seen by their R^2 values, as there is variation along the y direction. The slowest setting consistently produces the least dense components at all locations, and the variation along the x direction is no longer significant when using the slow setting. This indicates that the trend is caused by the effects of increasing the flow velocity and not the flow pattern itself.

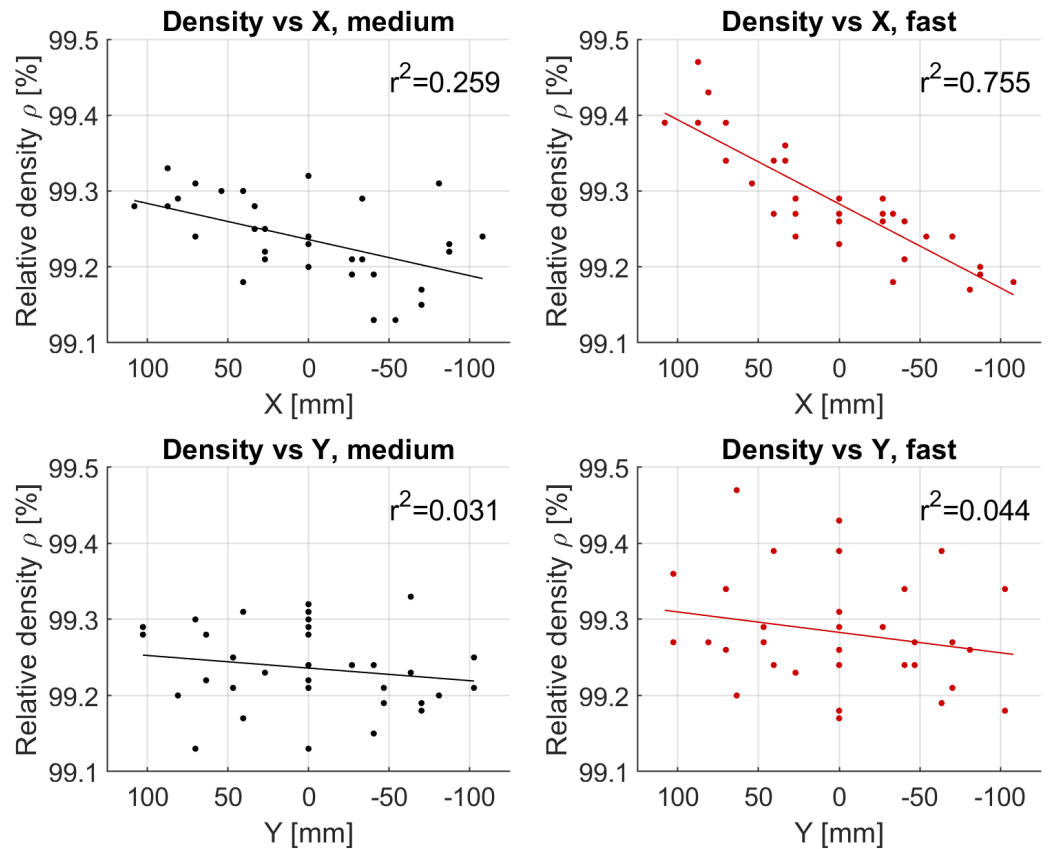


Figure 6. The relative bulk density of the samples concerning their positions on the build plate. The data is shown with a linear fit and corresponding r^2 .

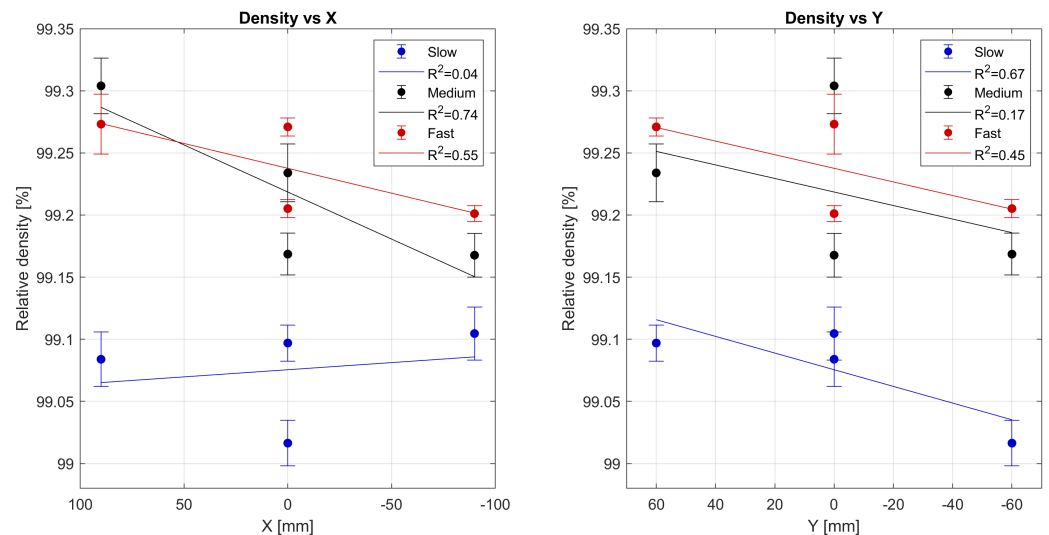


Figure 7. Densities of the clusters plotted in the X and Y directions, including the no-flow densities.

The density with respect to the y location reveals what is also seen from plotting with the x location: a difference in the density sideways relative to the flow. The left side of the flow ($y = -60$) is lower in density than the other side. Referring to Figure 3, the YZ plane reveals a pocket of lower velocity at $x = 0$. The slowest flow appears to have the slightest difference in densities in the x direction ($y = 0$), which coincides with the minor flow gradient of the three settings.

3.2.3. No Gas Flow

The observed variation regarding the cube samples was more minor than expected. In comparison, the cylinder showed significant differences between the slow setting and the fast and medium settings. It was decided to search for the limit to establish a baseline. To that end, an experiment was conducted with a zone with no gas flow. The samples' location on the build plate and their corresponding densities are seen in Figure 8. A stark difference is seen between the regions with and without flow (green vs. red), with the bottom-right image in Figure 8 showing the rising plume without flow present. In particular, at $x \approx 0$, the difference is 9% in the relative density between the slow and no-flow settings. The plume seen in Figure 8 interacts with the laser beam to a degree, whereby the beam illuminates the plume, appearing as a light curtain. The clusters at $y \approx 90$ and $y \approx -90$ show less variation. The cluster at $y \approx -90$ appears to be in a transition zone between little and no flow and fares better than the cluster deep in the no-flow zone. The cluster near the gas outlet yielded slightly less dense samples than the cluster in the green zone due to a similar transitional zone. Clearly, the flow is vital for producing dense components with industrial process parameters and avoiding damage to the optical components.

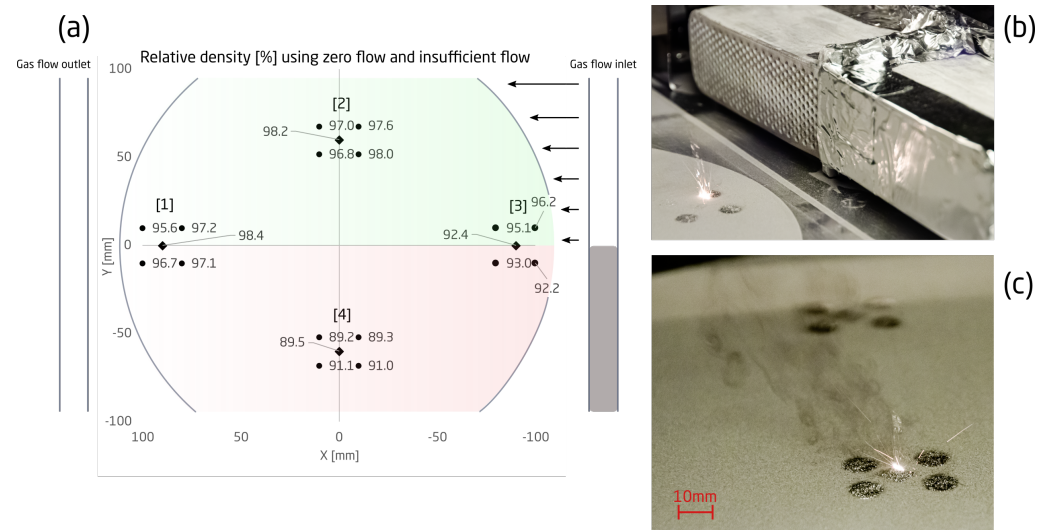


Figure 8. (a) Density results from manufacturing without a gas flow relative to the build plate location. (b) The covered inlet and the laser-plume interaction. (c) Plume formed at the cluster in the no-flow zone ($x = 0, y = -60$).

3.3. Melt Pools

The melt pools measured at the top layer in the slow-flow and no-flow experiments directly show the impact of a poor gas flow on the microstructure, ultimately leading to unsatisfactory densities and mechanical properties. Besides a significant lack of fusion porosities (Figure 9e,d), the melt pools undergo a stark transformation. The melt pool's average width increases slightly and decreases in depth, resulting in shallow melt pools, as also shown in Figure 10. In particular, the samples deep in the no-flow zone experience a decrease in penetration depth as the effective energy input is reduced due to the byproducts scattering the laser, as introduced in Sections 1.2 and 1.3. Furthermore, the redeposited spatter particles form inclusion porosities.

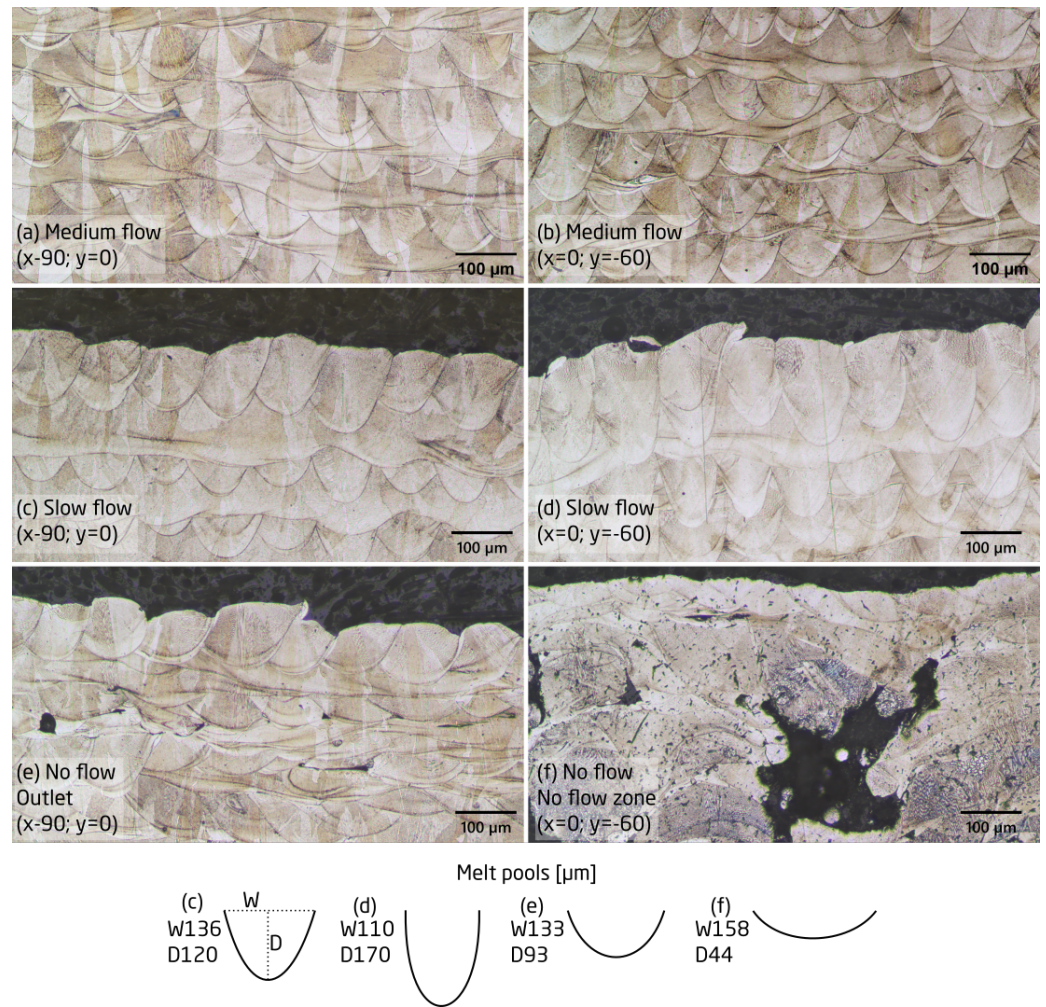


Figure 9. Light Optical microscopy micrographs of cross sections of select samples. Medium flow: (a,b). Slow flow: (c,d). No flow at the outlet: (e) at the outlet. No-flow zone (f). Melt pool morphology and corresponding average dimensions in micrometers are illustrated below.

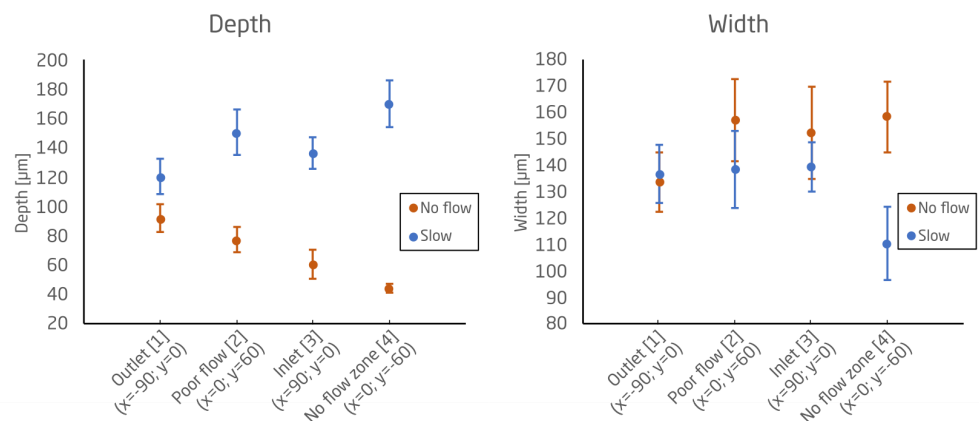


Figure 10. Melt pool measurements under the slow-flow and no-flow conditions.

3.4. Summary

Figures 6 and 7 reveal an issue with the local flow conditions near the gas inlet. This is likely due to a turbulent region near the inlet that appears to increase with a faster flow. Swirling of the plume was observed when processing near the inlet. Similar behavior was observed by Elkins et al. [22] using magnetic resonance imaging, where vortices were observed near the gas inlet due to the backward-facing step-flow effect caused by the inlet

being elevated above the surface. The separation region below the flow is bounded by the bottom surface, causing surrounding gas to be sucked into the separation region, which can cause vortices. According to the XZ planes in Figure 3, the distance from the inlet to the reattachment zone with the fast setting appears to be approximately 70 mm from the build plate center, which would affect the outermost samples located 90 mm from the center. This is a substantial area where conditions may be subpar. Decreasing the step height (distance from the flow to the bottom surface) and increasing the inlet distance to the processing area can negate the impact of the step-flow effect on the process. Decreasing the velocity may decrease the step effect, all the while having a detrimental impact on the rest of the processing area, in agreement with the lower-density gradient along the x direction in Figure 6.

Clearly, the energy input is directly affected by the flow and appears to be decreased to a degree where the melt pool depths are reduced by approximately a factor of four. Furthermore, significant porosities in the no-flow zone are present, indicating an unstable and chaotic process.

4. Discussion and Conclusions

The experimental flow map method is suitable for quantifying the gas flow conditions and encompasses the entire flow path and the blower and filter characteristics. The used flow probe was available and easy to use; however, certain hot-wire anemometers can characterize turbulence, which would be beneficial in analyzing the flow, particularly near the flow inlet. Increasing the area of data collection near the inlet and outlet would also help crystallize the flow behavior.

The gas flow significantly impacts the manufactured components, and great care must be taken when designing the shielding gas subsystem. The samples produced in the region without flow resulted in bulk densities below 90% and 98.2% under poor and no-flow conditions, respectively. By increasing the flow velocity, it was possible to increase the bulk density of the manufactured components. Using different flow settings, the samples resulted in a range of 99.0–99.3% at the same locations using identical process parameters. The highest density attained was nearly 99.5% using slightly higher energy densities.

The fast flow setting resulted in mean velocities per measured plane ranging from $z_0 = 1.7$ m/s to $z_{25} = 3.4$ m/s, whereas the medium setting ranged from $z_0 = 1$ m/s to $z_{25} = 1.8$ m/s. However, the gain in bulk density was small, at best, and mostly insignificant. Furthermore, micrographs did not reveal differences between the samples. However, the melt pools of the slow- and no-flow conditions showed significant disparities. The slow setting ranging from $z_0 = 0.3$ m/s to $z_{25} = 0.5$ m/s was detrimental to the sample densities but still yielded deeper melt pools compared to the no-flow experiment. The gas flow directly affects the resulting energy input into the powder bed. While diminishing returns may be seen going from medium to fast at the current state of the gas subsystem (where certain regions benefit and others suffer from increasing the flow velocity), the slow setting with average velocities below 1 m/s is unacceptable.

The spatially differential disparities are hypothesized to be due to turbulence and vortices formed near the inlet, which may prevent the plume from being removed and cause powder denudation. When processing near the inlet, the plume was observed to be sucked toward the flow inlet. Powder denudation was not analyzed in this work; however, it may be present throughout the processing area and could also play a part in the relative increase in density away from the inlet [12]. As the fast setting produced more dense samples overall, it is not likely to be a critical issue.

In future work, the flow geometry will be redesigned to move the inlet closer to the build plate [20] and further away from the processing area to reduce the step effect [22]. We will also investigate how to alleviate the low-velocity pocket on the left side of the flow at $x = 0$.

- Based on the results, it is recommended to use a shielding cross flow with a minimum average velocity at the build plate of 1 m/s under the assumption of a uniform flow;

- It is recommended to keep the height of the inlet from the bottom surface as low as possible, keeping in mind the distance to the processing area;
- Flow conditioners are necessary for a smooth and directionally stable flow across the build plate [23,26].

Author Contributions: Conceptualization, M.B.K., Z.P. and V.K.N.; methodology, M.B.K., Z.P. and V.K.N.; software, M.B.K.; validation, M.B.K., Z.P. and V.K.N.; formal analysis, M.B.K. and V.K.N.; investigation, M.B.K. and Z.P.; resources, V.K.N. and D.B.P.; writing—original draft preparation, M.B.K.; writing—review and editing, V.K.N. and D.B.P.; visualization, M.B.K.; supervision, V.K.N. and D.B.P.; funding acquisition, D.B.P. All authors have read and agreed to the published version of the manuscript.

Funding: This research was funded by the Poul Due Jensen Foundation (grant number 2018-017).

Data Availability Statement: Data will be available upon request. Please refer to the project's <https://github.com/DTU-OpenAM/OpenAM-PBF> for more information regarding the L-PBF system and source.

Acknowledgments: The authors wish to thank Moritz Zwicker for his contribution to the early stages of the data analysis.

Conflicts of Interest: The authors declare no conflict of interest. The funders had no role in the design of the study; in the collection, analyses, or interpretation of data; in the writing of the manuscript; or in the decision to publish the results.

Abbreviations

The following abbreviations are used in this manuscript:

L-PBF	Laser powder bed fusion
AM	Additive manufacturing
VED	Volumetric energy density
NC	Numerical control

References

1. Zhang, Y.; Wu, L.; Guo, X.; Kane, S.; Deng, Y.; Jung, Y.G.; Lee, J.H.; Zhang, J. Additive Manufacturing of Metallic Materials: A Review. *J. Mater. Eng. Perform.* **2018**, *27*, 1–13. [CrossRef]
2. Ladani, L.; Sadeghilaridjani, M. Review of Powder Bed Fusion Additive Manufacturing for Metals. *Metals* **2021**, *11*, 1391. [CrossRef]
3. Culmone, C.; Smit, G.; Breedveld, P. Additive manufacturing of medical instruments: A state-of-the-art review. *Addit. Manuf.* **2019**, *27*, 461–473. [CrossRef]
4. Blakey-Milner, B.; Gradl, P.; Snedden, G.; Brooks, M.; Pitot, J.; Lopez, E.; Leary, M.; Berto, F.; du Plessis, A. Metal additive manufacturing in aerospace: A review. *Mater. Des.* **2021**, *209*, 110008. [CrossRef]
5. Wohlers, T.T.; Campbell, I.; Diegel, O.; Huff, R.; Kowen, J. *Wohlers Report 2022: 3D Printing and Additive Manufacturing Global State of the Industry*; Technical Report; ASTM International: West Conshohocken, PA, USA, 2022.
6. Scipioni Bertoli, U.; Wolfer, A.J.; Matthews, M.J.; Delplanque, J.P.R.; Schoenung, J.M. On the limitations of Volumetric Energy Density as a design parameter for Selective Laser Melting. *Mater. Des.* **2017**, *113*, 331–340. [CrossRef]
7. Ahmed, N.; Barsoum, I.; Haidemenopoulos, G.; Al-Rub, R.K. Process parameter selection and optimization of laser powder bed fusion for 316L stainless steel: A review. *J. Manuf. Process.* **2022**, *75*, 415–434. [CrossRef]
8. Bidare, P.; Bitharas, I.; Ward, R.M.; Attallah, M.M.; Moore, A.J. Fluid and particle dynamics in laser powder bed fusion. *Acta Mater.* **2018**, *142*, 107–120. [CrossRef]
9. Bitharas, I.; Burton, A.; Ross, A.J.; Moore, A.J. Visualisation and numerical analysis of laser powder bed fusion under cross-flow. *Addit. Manuf.* **2021**, *37*, 101690. [CrossRef]
10. Tenbrock, C.; Kelliger, T.; Praetzs, N.; Ronge, M.; Jauer, L.; Schleifenbaum, J.H. Effect of laser-plume interaction on part quality in multi-scanner Laser Powder Bed Fusion. *Addit. Manuf.* **2021**, *38*, 101810. [CrossRef]
11. Reijonen, J.; Revuelta, A.; Riipinen, T.; Ruusuvoori, K.; Puukko, P. On the effect of shielding gas flow on porosity and melt pool geometry in laser powder bed fusion additive manufacturing. *Addit. Manuf.* **2020**, *32*, 101030. [CrossRef]
12. Shen, H.; Rometsch, P.; Wu, X.; Huang, A. Influence of Gas Flow Speed on Laser Plume Attenuation and Powder Bed Particle Pickup in Laser Powder Bed Fusion. *J. Miner. Met. Mater. Soc.* **2020**, *72*, 1039–1051. [CrossRef]
13. Ion, J.C. *Laser Processing of Engineering Materials: Principles, Procedure and Industrial Application*; Elsevier: Boca Raton, FL, USA, 2005; pp. 1–556.

14. Wang, D.; Wu, S.; Fu, F.; Mai, S.; Yang, Y.; Liu, Y.; Song, C. Mechanisms and characteristics of spatter generation in SLM processing and its effect on the properties. *Mater. Des.* **2017**, *117*, 121–130. [[CrossRef](#)]
15. Ladewig, A.; Schlick, G.; Fisser, M.; Schulze, V.; Glatzel, U. Influence of the shielding gas flow on the removal of process by-products in the selective laser melting process. *Addit. Manuf.* **2016**, *10*, 1–9. [[CrossRef](#)]
16. Taylor, H.C.; Wicker, R.B. Impacts of microsecond control in laser powder bed fusion processing. *Addit. Manuf.* **2022**, *60*, 103239. [[CrossRef](#)]
17. Stokes, M.A.; Khairallah, S.A.; Volkov, A.N.; Rubenchik, A.M. Fundamental physics effects of background gas species and pressure on vapor plume structure and spatter entrainment in laser melting. *Addit. Manuf.* **2022**, *55*, 102819. [[CrossRef](#)]
18. Ghasemi-Tabasi, H.; Jhabvala, J.; Boillat, E.; Ivas, T.; Drissi-Daoudi, R.; Logé, R.E. An effective rule for translating optimal selective laser melting processing parameters from one material to another. *Addit. Manuf.* **2020**, *36*, 101496. [[CrossRef](#)]
19. Weaver, J.S.; Schlenoff, A.; Deisenroth, D.C.; Moylan, S.P. *Inert Gas Flow Speed Measurements in Laser Powder Bed Fusion Additive Manufacturing*; NIST Advanced Manufacturing Series 100-43; National Institute of Standards and Technology: Gaithersburg, MD, USA, 2021. [[CrossRef](#)]
20. Zhang, X.; Cheng, B.; Tuffile, C. Simulation study of the spatter removal process and optimization design of gas flow system in laser powder bed fusion. *Addit. Manuf.* **2020**, *32*, 101049. [[CrossRef](#)]
21. Cattafesta, L.; Bahr, C.; Mathew, J. Fundamentals of Wind-Tunnel Design. In *Encyclopedia of Aerospace Engineering*; Wiley Online Library: Hoboken, NJ, USA, 2010. [[CrossRef](#)]
22. Elkins, C.; Mireles, J.; Estrada, H.; Morgan, D.; Taylor, H.; Wicker, R. Resolving the Three-Dimensional Flow Field within Commercial Metal Additive Manufacturing Machines: Application of Experimental Magnetic Resonance Velocimetry. *Addit. Manuf.* **2023**, *75*, 103651. [[CrossRef](#)]
23. Yang, Y.; Chen, Z.; Liu, Z.; Wang, H.; Zhang, Y.; Wang, D. Influence of shielding gas flow consistency on parts quality consistency during large-scale laser powder bed fusion. *Opt. Laser Technol.* **2023**, *158*, 108899. [[CrossRef](#)]
24. Schniedenharn, M.; Wiedemann, F.; Schleifenbaum, J.H. Visualization of the shielding gas flow in SLM machines by space-resolved thermal anemometry. *Rapid Prototyp. J.* **2018**, *24*, 1296–1304. [[CrossRef](#)]
25. Philo, A.M.; Sutcliffe, C.J.; Sillars, S.; Sienz, J.; Brown, S.G.; Lavery, N.P. A study into the effects of gas flow inlet design of the Renishaw AM250 laser powder bed fusion machine using computational modelling. In *Proceedings of the Solid Freeform Fabrication 2017: Proceedings of the 28th Annual International Solid Freeform Fabrication Symposium—An Additive Manufacturing Conference, SFF 2017, Austin, TX, USA, 7–9 August 2017*; pp. 1203–1219.
26. Kjer, M.B.; Zwicker, R.L.; Nadimpali, V.; Pedersen, D.B. Experimental Analysis and Optimization of Gas Flow in an Open-Architecture Metal L-PBF System. In *Proceedings of the 33rd Annual International Solid Freeform Fabrication (SFF) Symposium, Austin, TX, USA, 25–27 July 2022; Volume 33*, pp. 1321–1330.

Disclaimer/Publisher’s Note: The statements, opinions and data contained in all publications are solely those of the individual author(s) and contributor(s) and not of MDPI and/or the editor(s). MDPI and/or the editor(s) disclaim responsibility for any injury to people or property resulting from any ideas, methods, instructions or products referred to in the content.